







Synthesis of nanocrystalline boron ion doped SnO₂ and its morphology dependent anti-microbial activity

Sujay Munshi¹ , Solanki Das², Achyutmohan Roychaudhury² ,
Aritra Banerjee³ , Debtanu Ghosh⁴ , Partha Chatterjee⁴ ,
Apurba Kanti Deb^{1,*} 

¹Department of Physics, Raiganj University, Raiganj, Uttar Dinajpur, India.

²Department of Chemistry, Raiganj University, Raiganj, Uttar Dinajpur, India

³Department of Physics, University of Calcutta, 92 A P C Road, Kolkata, India.

⁴Department of Physics, Vivekananda Mahavidyalaya, Haripal, Hooghly, India.

*Corresponding author: deb.apurba@gmail.com

Original Research

Abstract:

Received:
13 December 2023
Revised:
20 March 2024
Accepted:
7 May 2024
Published online:
25 May 2024

Boron doped tin oxide nanocrystals with tetragonal symmetry (space group: $P4_2/mnm$) were prepared by sol-gel route using three different polyhydroxy alcohols like starch, glycerol and poly vinyl alcohol (PVA). Morphological and structural properties were studied for these samples by using scanning electron microscopy, X-ray powder diffraction, Raman spectroscopy and Fourier transform infrared spectroscopy. The morphology of the as-prepared SnO₂ sample is dependent on the polyhydroxy alcohol used for preparation in sol-gel method and is evident from scanning electron microscopy and X-ray powder diffraction line profile analysis. Detailed characterization for the effects of lower particle dimensions has been explored and existence of oxygen vacancies has been observed for all the samples. Paracrystalline disorder was observed in the SnO₂ sample prepared in glycerol medium. Boron is present as interstitial BO₄ and BO₃ unit in crystal lattice. The anti-bacterial efficacy of the boron doped SnO₂ samples is dependent on the crystallite morphology.

© The Author(s) 2024

Keywords: Antibacterial activity; Boron ion doped SnO₂ nanoparticles; FTIR; Raman spectroscopy; X-ray powder diffraction line profile analysis

1. Introduction

Semiconductor metal oxides (MSO) have kindled much interest amongst the researchers during the last few years due to their intriguing properties and applications in diverse fields. These materials exhibit significant change in their properties on going from the bulk to the nanocrystalline form as well as upon doping with suitable metallic or non-metallic elements. Amongst these semiconductor metal oxides, tin oxide has caught huge attention in recent years for their potential application in photocatalytic activity [1–3], gas sensing [4–7], energy storage [8], optoelectronic applications [9, 10], photovoltaic properties [11], lithium ion batteries [12–15], electronic devices [16], thermoelectric properties [17], magnetic properties [18, 19], biological efficacy [2, 20] etc. to mention a few.

Under ambient condition the stable phase of tin oxide is

SnO₂, possessing tetragonal rutile crystal structure and is an n-type large band gap semiconductor with a high degree of transparency in the visible range [21–23]. Several efficient methods have been used to synthesize SnO₂ nanoparticles in pure form and also doped SnO₂ nanoparticles to govern/modify its microstructural and physicochemical properties. These methods include hydrothermal method [24], polymeric [25], organo-metallic precursor synthesis [26], sonication [27], microwave [28, 29], spray pyrolysis [30, 31], sol-gel [32, 33] etc. Amongst these methods sol-gel method has advantages over other method methods in terms of its simplicity, low processing temperature, flexibility of forming dense monoliths and nanoparticles. In a sol-gel method the solution is transformed into an inorganic solid by dispersion of colloidal particles in a liquid (sol) and conversion of sol into rigid phase (gel) by hydrolysis and condensation

reaction. Generally this leads to synthesis of amorphous precipitates followed by heat treatment for re-crystallization and different microstructure.

Investigations on boron doped SnO₂ both in microcrystalline and nanocrystalline forms are rare. There are few research works on structural, electrical and optical properties of boron-doped SnO₂ in powder form and thin films [34–38]. Kumar and his co-researchers [35] have synthesized boron-doped SnO₂ nanoparticles in crystalline rutile phase via wet chemical method. They have showed the ability of these nanoparticles in photocatalytic hydrogen generation by water splitting and degradation of different dyes due to the defect and oxygen vacancies generated by doping of boron atom. From first-principle calculation, Yu et.al. [39] have studied structural and electronic properties of SnO₂ when doped with non-metallic elements including boron. They have found slight lattice expansion and modification in energy band gap upon doping with B. This results in increase in the conductivity of SnO₂ crystal. The effect of structural, electrical and optical properties on boron content in tin oxide thin films prepared by sol-gel dip coating on glass substrate were investigated and found as suitable candidate for transparent conducting oxide (TCO) applications [36]. By applying the density functional theory calculations, Fillppatos et.al. [40] have made a comparative study and examined the impact of B and In doping on the structural, electrical and optical properties of SnO₂. They have investigated the role of dopant in the interstitial/ substitutional site on the modification of energy band gap and concluded their usefulness in photocatalytic applications. However till date the present authors have not encountered any scientific article investigating the dependence of microstructural and morphological characteristics of B-doped SnO₂ by sol-gel method and its influence on bacterial inhibition activities. In this paper, we have intended to report the role of polyhydroxy alcohols on the microstructural features and polycrystalline disorder of boron doped SnO₂ nano-materials and hence the effects on their antimicrobial efficacy. A comprehensive structural, microstructural and morphological characterization have been done by employing Scanning Electron Microscopy (SEM), X-ray Powder Diffraction (XRPD), Raman Spectroscopy, and Fourier Transform Infrared Spectroscopy (FTIR). Further we have explored the dependence of antimicrobial efficacy of B-doped SnO₂ samples prepared in different polyhydroxy alcohols having different microstructural features against two distinct kinds of bacteria. In this work we have chosen *E. Coli* and *E. Aerogens*, being Gram-negative bacteria, having thin layered peptidoglycan cell walls and hence appear red under gram staining whereas another *Staphylococcus Aureus*, a Gram-positive bacteria, has thick cell wall and shows violet colour under gram staining.

2. Materials and methods

2.1 Sample preparation

Boron doped SnO₂ was prepared by dissolving 1.140 gm stannous chloride (SnCl₂·2H₂O, AR grade, Merck) in 50 mL dilute hydrochloric acid. Then 1:1 ammonium hydroxide was added to it drop by drop until tin hydroxide precipi-

tates completely. The white precipitate was filtered through Gooch crucible with sintered disc (G4) followed by washing with warm distilled water. Then the precipitate of tin hydroxide was mixed with 0.251 g of boric acid (H₃BO₃, AR grade, SRL). Then mixture of tin hydroxide and boric acid was added to starch solution, which was prepared using 2 g of starch (potato starch; extra pure, SDFCL) and 100 mL of distilled water by boiling. The mixture was then stirred on a magnetic stirrer for 3 hours at 80 °C until it was converted from sol to gel. The gel was dried nearly to dryness. After that, ignition of the dried mass was done by keeping it in silica crucible and heated in a muffle furnace at 800 °C for 2 hours. The prepared material, hereafter, is referred to as BTO1.

BTO2 and BTO3 are prepared by same procedure but using glycerol (AR grade, Merck) solution (100 mL glycerol + 50 mL distilled water) and PVA (MW: 115000; Loba Chemie) solution (2 g PVA in 100 mL distilled water) respectively instead of starch.

2.2 Sample characterization

Field emission scanning electron microscopy (FESEM) images of the samples were recorded in M/s Carl Zeiss, Sigma 300 and the elemental distribution/mapping is revealed from respective FESEM energy dispersive X-ray (EDX) spectrum. The X-ray powder diffraction patterns of the synthesized boron doped SnO₂ samples were taken at room temperature in a X'Pert PRO Diffractometer (PW 3040/60, PANalytical) operating at 45 kV and 40 mA, using Ni filtered CuK_α radiation. Step scan with a step size of 0.02° 2θ and the counting time of 5 sec per step were recorded within the 2θ range 20° - 120° for having good signal to noise ratio. The instrumental profile was determined from the diffraction pattern of Si standard [41], recorded with similar slits system. Raman measurements were performed in backscattering geometry using Lab RAM HR (JobinYvon) spectrometer equipped with argon ion (Ar⁺) laser of wavelength 488 nm. Raman scattering measurements for the powder samples were performed at room temperature in the range from 50 to 1000 cm⁻¹. The Fourier transformed infrared (FTIR) spectra of the samples were collected using a IRAffinity-1S, Shimadzu, FTIR spectrophotometer in the range (400 – 4000) cm⁻¹ for all three of the samples.

2.3 Anti-microbial activity

Agar disc diffusion method ([20] and references there in) was used to explore the antibacterial activities of the boron doped tin oxide samples in vitro against two Gram-negative bacteria *Escherichia Coli* (MCC2413), *Enterobacter Aerogens* (MCC3092) and one Gram-positive bacteria *Staphylococcus Aureus* strains by NCCLS (National Committee for Clinical Laboratory Standards, 1997, India). The nutrient agar (Hi-Media Laboratories Limited, Mumbai, India), was autoclaved at 121 °C at 1 atmosphere pressure for 15 – 20 minutes. The sterile-nutrient media was kept at 45 - 50 °C. Then 100 μL of bacterial suspension containing 10⁸ colony forming units (CFU)/mL were mixed with sterile liquid nutrient agar and poured into the sterile petri dishes. Upon solidification of the media, filter disc (5 mm diameter) was individually soaked with concentration of 500 μg/mL of

each compound and placed on the nutrient agar media plates. The plates were incubated for 24 h at 37 °C. The diameter of the zone of inhibition (including disc diameter of 5 mm) was measured. Each experiment was performed in triplicate to minimize errors and the mean values were accepted.

3. Results and discussion

3.1 EDX and FESEM study

Energy dispersive X-ray spectroscopy spectrum of the synthesized doped BTO samples BTO1 and BTO3 are shown in Fig. 1. Similar spectrum have been observed for BTO2 sample (not shown for brevity). EDX spectrum for all the three *B* doped SnO₂ confirmed the presence of the elements Sn and O. For BTO1, the weight and atomic percentage of Sn:O are 90.18:9.82 and 56.98:43.02, whereas for BTO3, these ratios are 83.14:16.86 and 40.41:59.59 respectively. However as evident from Fig. 1, the presence of boron could not be established from the EDX spectrum. This might be due to lower peak intensity for low production of X-rays and large self-absorption for the lighter element boron.

The particle dimensions and morphologies are shown in field emission electron microscopy images (in Fig. 2). From Fig. 2 it appears that the particle morphologies for the samples BTO1 and BTO2 are isotropic i.e. almost spherical in shape. However for the boron doped sample BTO3, particle morphologies are anisotropic in nature. Particle size distributions for the three samples are shown in the inset. The mean particle sizes thus obtained from the distribution for BTO1 and BTO2 are 16 nm and 34 nm respectively, whereas for BTO3, though anisotropic in nature, is around 49 nm.

3.2 X-ray powder diffraction analysis

The X-ray powder diffraction (XRPD) line profile can be described as a convolution of ‘true’ specimen and the instrumental broadening. Mathematically, it can be expressed as [42]

$$Y_c(2\theta) = [B * (I_S * I_A)](2\theta) + Bkg \quad (1)$$

where the ‘true’ sample broadening function, represented by B , I_S and I_A corresponds to the symmetric and anti-symmetric part of the instrumental broadening function,

present in the incident beam for mainly the slit systems used. The background function Bkg is modeled using polynomial of degree 4 to take care of the fluctuation at the non-Bragg positions [43]. The X-ray powder diffraction patterns in the range 20 – 120° 2θ for three boron doped tin oxide samples synthesized in different polyhydroxy alcohols are shown the Fig. 3. The diffraction patterns in all cases show the reflections of SnO₂ with tetragonal symmetry having space group $P4_2/mnm$ (JCPDS file number 41-1445). No traces of boron and/or boron oxide could be identified from the diffraction pattern and hence it can be concluded that the dopant atom *B* has occupied interstitial/substitutional sites in the tetragonal lattice of SnO₂. However, small presence of boron oxide as vitreous state cannot be completely ruled out.

As a part of preliminary investigation, the individual reflections of each diffraction pattern were fitted with a pseudo-Voigt function [44]. The peak position, intensity, FWHM and pseudo-Voigt mixing parameter were held as refinable parameters. The integral breadth β of each diffraction line profile were calculated from the refined values of profile fitting parameters. Fig. 4 shows the classical Williamson–Hall plot (WH plot) of total integral breadth $\beta^*(= \beta \cos \theta / \lambda)$ as a function of $d^*(= 2 \sin \theta / \lambda)$ for the all the specimen. From the visual inspection of the extent of broadening in the WH plot, it is clear that the sample BTO1, having larger broadening, has the smallest coherent domain size amongst the three, in contrast with the doped SnO₂ sample BTO3. The most significant finding from Fig. 4 is that although the progression of the profile broadening with the diffraction vector is almost linear for samples BTO1 and BTO2, but β^* shows scattered and global dependence on d^* for BTO3. This immediately reflects isotropic size-strain broadening for the samples BTO1 and BTO2. The crystallite morphology is anisotropic for the doped SnO₂ sample BTO3 prepared in PVA. Further the nature of linear variation of β^* vs d^* for BTO2 and BTO1 indicates that the microstructural broadening is predominantly due to smaller isotropic crystallites. To elucidate these different microstructural characteristics a detail structural and microstructural analysis have been done using modified Rietveld method for the three boron

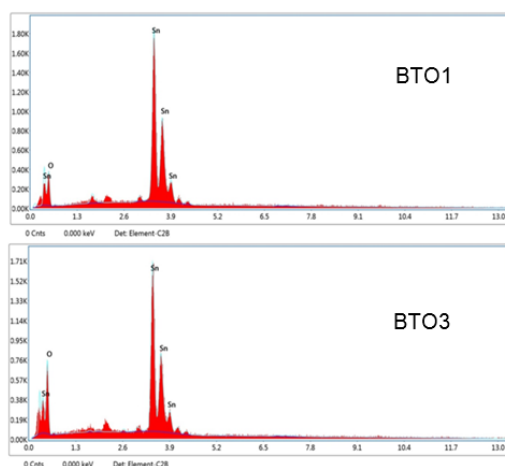


Figure 1. EDX spectrum of BTO1 and BTO3 samples.

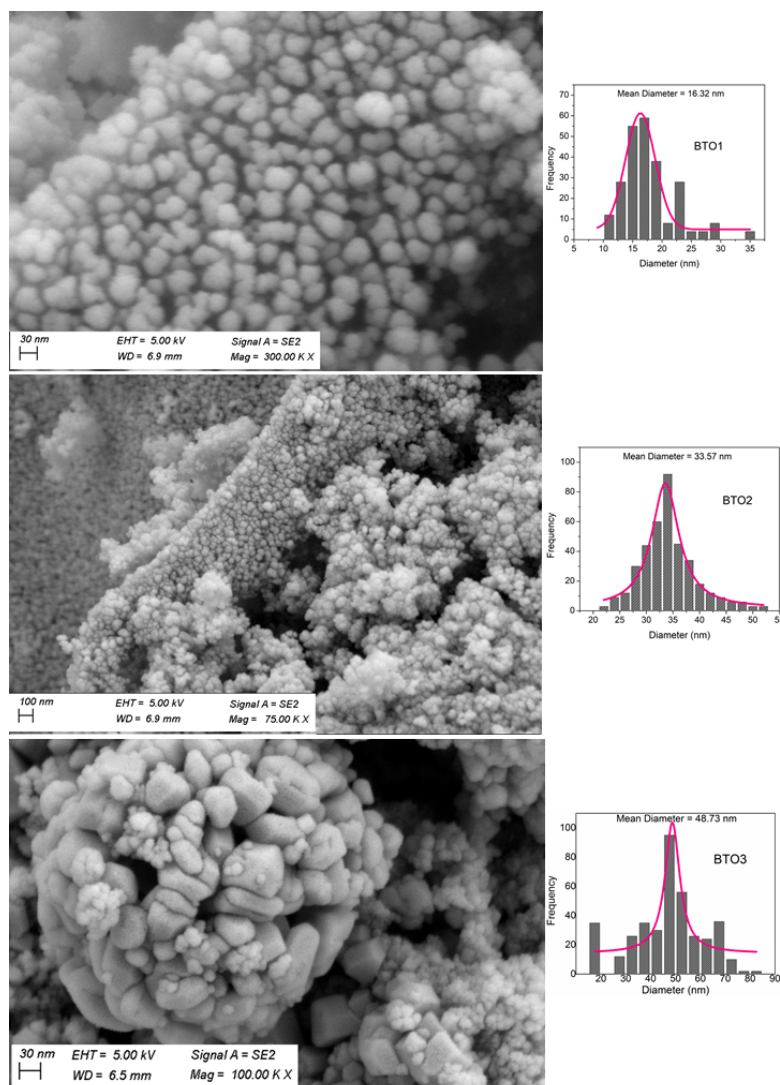


Figure 2. The FESEM images of the synthesized SnO_2 samples (a) BTO1 (b) BTO2 and (c) BTO3.

doped tin oxide samples.

The prerequisite for whole profile fitting Rietveld analysis is to identify the phase and start with reasonably close values of cell parameters, atomic positions followed by choice of microstructural model apt for the material concerned. In modified Rietveld analysis the microstructural features are also included as refinable parameters to evaluate the profile shape parameters theoretically along with the other adjustable structural parameters like unit cell parameters, atomic positions etc. All these structural and microstructural refinement features have been incorporated in several useful softwares. Here, one such software MAUD [42] has been used as it also allows modeling the anisotropic microstructure by using the most amenable approach given by Popa [45], where for different Laue classes, the average radii of the anisotropic crystallites along different (hkl) directions are treated as convergent series of spherical harmonics. In MAUD the whole diffraction pattern is fitted simultaneously with pseudo-Voigt type profile shape function. Here a fourth order polynomial was considered to account for the background diffraction patterns of BTO2

and BTO3, however a fifth order polynomial was chosen to describe the relatively larger fluctuating background of XRPD pattern for the sample BTO1. As obtained from preliminary investigation, two different microstructural models were assumed for the boron doped nanocrystalline tin oxide samples, the isotropic size-strain model for BTO1 and BTO2 but for BTO3 the size-strain model considered was anisotropic following Popa rule. Refined values of structural parameters, size-strain values and other microstructural features as obtained from Rietveld analysis are presented in Table 1. As also indicated from the individual line profile analysis (WH plot), Rietveld analysis shows that BTO1 has the smallest particle size of ~ 12 nm and BTO2 has the largest strain $\sim 17 \times 10^{-4}$. For BTO3 it has been observed that the fitted pattern represents the observed pattern more closely when the anisotropic microstructural model was taken. The standard deviations of different refined parameters, reliability parameters and hence the goodness-of-fit (Gof) are lowered in comparison to that obtained by considering isotropic size-strain model as taken in case of BTO1 and BTO2. The size-strain values for BTO3 along differ-

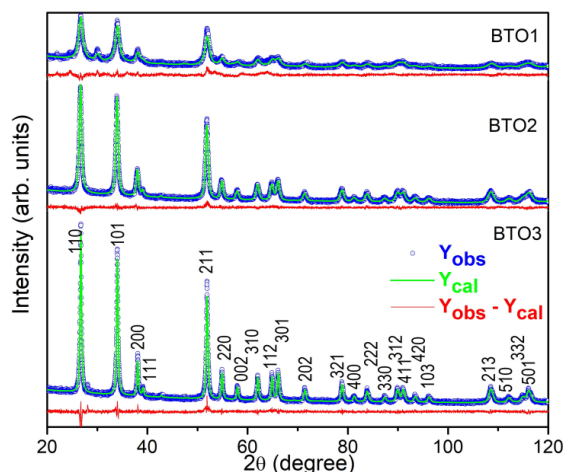


Figure 3. Rietveld fitted X-ray powder diffraction pattern of the three boron doped tin oxide samples along with the residuals.

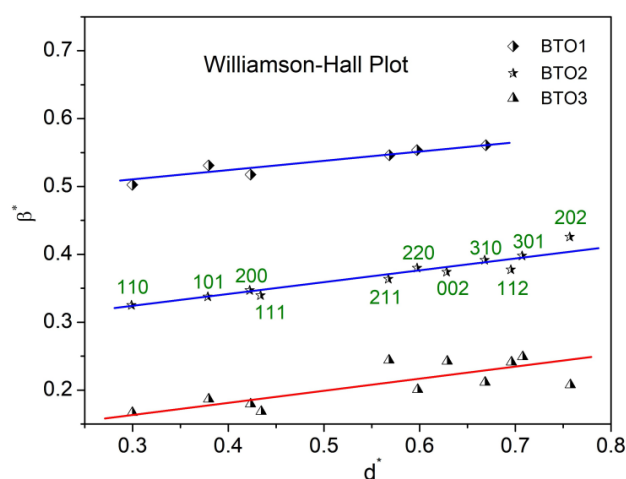


Figure 4. Williamson-Hall plot of B doped SnO₂ samples revealing their different microstructural features.

ent (hkl) directions are given in Table 1. The microstrain values of BTO3 samples are the lowest. Further to estimate the presence of oxygen vacancies in these nanocrystalline BTO samples, the occupancy of O atom was refined independently. Amongst the three boron doped SnO₂ samples the occupancy became least for the smallest BTO1 and the value refined to ~ 0.92. For the other two samples the occupancy factor was refined to ~ 0.97 from unity. Hence, these nanocrystalline boron ion doped SnO₂ samples have oxygen deficiency which might have arisen due to surface effect and also for the incorporation of boron (B³⁺) in the lattice in place of the host cation (Sn⁴⁺).

It has been shown recently [46] that the lattice disorders in nanocrystalline samples are paracrystalline in nature. The nanoparticles are generally atomic clusters with different

sizes and different degree of disorder. In general there can be slight changes of lattice parameter. In the present case the refined values of the lattice parameter are slightly higher than that of pristine SnO₂. In order to investigate the nature of lattice disorder present in the doped SnO₂ samples it is required to analyze at least three orders of a given hkl reflection. It has been shown by Hoseman [47] that a distinction between the lattice disorder of first kind (viz. microstrain) and lattice disorder of second kind (viz. paracrystallinity) can be made by plotting the integral breadth as a function of the order number n of the hkl reflection. If the β* versus n plot is linear then microstrains are present. If on the other hand the plot between β* and n² is linear then paracrystalline distortion is present. The crystallite size and the percentage paracrystalline disorder coefficient g are

Table 1. Structural and microstructural parameters obtained from the Rietveld analysis of X-ray powder diffraction pattern for the synthesized BTO samples.

Sample	BTO1	BTO2	BTO3
<i>a</i> :	4.7393(6)	4.7394(2)	4.7391(7)
Cell (Å) <i>c</i> :	3.1837(5)	3.1878(1)	3.1868(7)
Size (nm)	12(1)	24(1)	31(110), 30(101), 26(200), 35(211), 31(220), 30(310)
Strain (×10 ⁴)	7.0(0.3)	17.2(0.3)	2.0(110), 1.3(101), 2.6(200), 1.3(211), 2.0(220), 2.4(310)
O _x	0.2981(11)	0.2992(6)	0.2972(6)
B _{iso} Sn	0.373(11)	0.160(13)	0.369(14)
B _{iso} O	0.373	0.160	0.369
O _{occupancy}	0.923(18)	0.972(8)	0.966(9)
Cell vol. (Å ³)	71.509	71.603	71.573
(<i>c/a</i>) ratio	0.672	0.673	0.672
R _{wp}	6.637	5.630	5.937
R _b	5.158		4.443
Gof	1.440		1.200
			4.415
			1.345

obtained from the following equation [47]

$$\beta = \frac{1}{D} + \frac{(\pi gn)^2}{D_{hkl}} \quad (2)$$

Fig. 5 shows the plot of between β^* and n^2 for the 110 planes for BTO2 sample. It may be mentioned here that in the present paper we have taken $n = (h^2 + k^2 + l^2)^{1/2}$. The plot is linear in nature indicating the presence of paracrystalline disorder in BTO2 sample. The calculated value of paracrystalline disorder along 110 is obtained to be 2%. The corresponding microstrain for the BTO2 sample is only 0.1% as evident from Table 1. For other two samples the slope the paracrystalline disorder is either absent or negligible. It is thus clear that glycerol medium produces slight paracrystalline disorder in the SnO₂ samples at least in the [110] direction. For the other two samples paracrystalline disorder could not established conclusively due to uncertainty of the profile parameters for the third order of the 110 reflection.

3.3 Raman and FTIR spectroscopy study

In the rutile structure of SnO₂ having $P4_2/mnm$ symmetry group, there are two tin atoms and four oxygen atoms in the unit cell. According to group theory, this six-atom unit cell gives rise to a total of 18 vibrational modes in the first Brillouin zone [48] which can be expressed as $\Gamma = A_{1g} + A_{2g} + B_{1g} + B_{2g} + E_g + 2A_{2u} + 2B_{2u} + 4E_u$. Amongst these phonon modes, A_{1g} , B_{1g} , B_{2g} and E_g are Raman active whereas A_{2u} and E_u vibration modes are active in the infrared region. The other modes A_{2g} and B_{1u} are silent and remaining A_{2u} and E_u modes are acoustic. In Raman active modes, the oxygen atoms vibrate and the tin atoms remain stationary. It has been reported that for SnO₂ single crystal in tetragonal rutile structure the Raman modes appear at 634 cm⁻¹ (A_{1g}), 123 cm⁻¹ (B_{1g}), 773 cm⁻¹ (B_{2g}) and 473 cm⁻¹ (E_g) [49]. The position of peaks of both Raman and IR spectra also depends on particle size of SnO₂ due to interaction of electromagnetic radiation with the shape and state of aggregation dependent size of nanoparti-

cles. It has been reported that for SnO₂ particle size of less than 7 nm, appears in the region of 50 – 100 cm⁻¹ belongs to B_{1g} mode of vibration [50], whereas classical vibration modes E_g , A_{1g} and B_{2g} appear in the high frequency region (450 – 775) cm⁻¹, for large sized particles. Fig. 6 shows the Raman spectra for the boron doped nanoparticles with different morphologies. The appearance of the phonon modes at 629 cm⁻¹, 771 cm⁻¹ and 471 cm⁻¹ corresponds to A_{1g} , B_{2g} and E_g respectively whereas the Raman band in the lower frequency region at 89 cm⁻¹ is assigned as B_{1g} mode of vibration. Existence of these Raman bands ensures the formation of tetragonal rutile structure of the doped SnO₂ nanoparticles. Intensity of the Raman peaks decreases and the peaks are also broadened with the reduction in particle size due to phonon confinement [51]. The strongest vibrational mode A_{1g} and also the phonon band B_{2g} are related to in-plane asymmetric vibration of Sn-O bonds [49]. Shifting of bonds and presence of the Raman active mode at 89 cm⁻¹ (B_{1g}), for the as-prepared samples, with particle size larger than 7 nm, signifies doping of boron into SnO₂ lattice [52]. Other than these typical Raman bands, presence of various other bands both in the lower wave number region as well as within 450 – 700 cm⁻¹ have been observed for all the doped SnO₂ nanoparticles. Several authors have identified these vibrational modes in pure and doped SnO₂ nanoparticles as a consequence of size effect, local disorder and surface defects like oxygen vacancies [53–57]. Dieguez et al. [48] predicted existence of non stoichiometric SnOx at the surface is responsible for the bands at 486 – 542 cm⁻¹ and 568 – 576 cm⁻¹ in nanocrystalline tin oxide. These phonon modes are labeled M₁ and M₂ in Fig. 6 (inset). The weak band appeared at 691 cm⁻¹ for BTO3 is attributed to IR active and Raman forbidden mode activated by disorder and surface defects present in the doped sample in nanometric form [48, 49]. It may be noted here that the Raman spectra of the BTO2 sample is distinctly different from the other two spectra. The spectrum of BTO2 is characterized by broad diffuse spectra. From the earlier section of XRD it is clear that BTO2 sample is characterized by paracrystalline

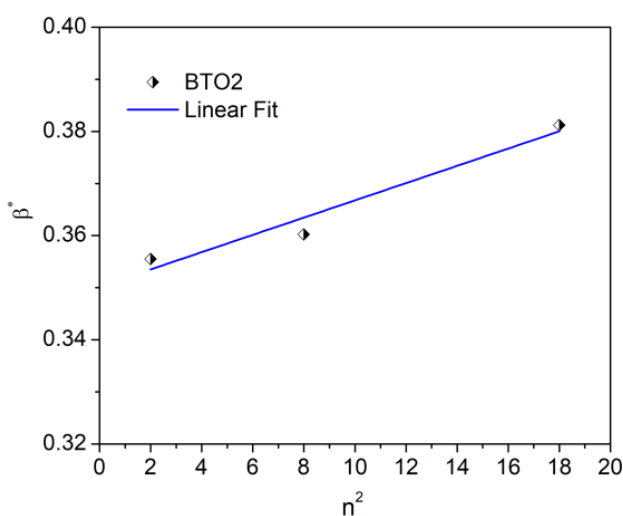


Figure 5. Plot of integral breadth β^* with n^2 for BTO2 sample for the 110 planes with linear fit.

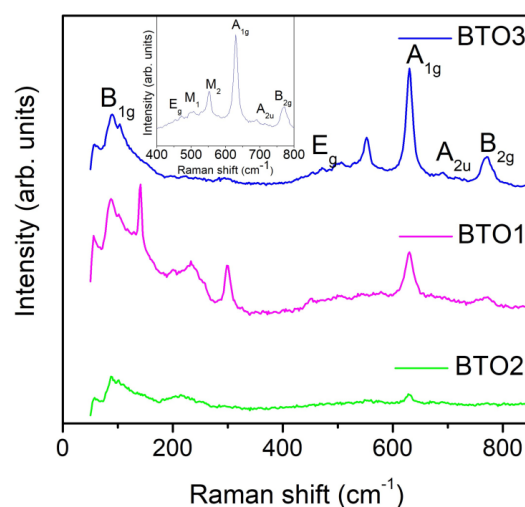


Figure 6. Raman spectra of the synthesized three BTO samples with different microstructure.

disorder. The broad and diffuse spectrum of BTO2 is consistent with such finding.

The functional groups present in the synthesized doped SnO₂ particles have been investigated by infrared spectra. Fig. 7 shows the room temperature FTIR spectra of the boron doped tin oxide nanocrystalline samples. The broad band, observed for all the samples in the wave number range (3116 – 3726) cm⁻¹, is attributed to stretching and bending vibration of surface –OH group due to the absorbed water during sample preparation [33, 49]. The sharp bands, appeared for all the doped SnO₂-nanoparticles at around 1620 cm⁻¹ and 1420 cm⁻¹, originate from the vibrational phonon modes *E_u* and *A_{2u}* respectively. Two other peaks, centered at 480 and 617 cm⁻¹, are the characteristic infrared absorption band for doped SnO₂ structure arising due to Sn–O and Sn–O–Sn vibrations respectively [2]. The broadness of the band at around 558 cm⁻¹ indicates the higher extent of surface defects in the crystal lattice [58] for all the samples BTO1, BTO2 and BTO3. As reported, the peaks at (600 – 660) cm⁻¹ correspond to the stretching mode of Sn–O–Sn [35]. The appearance of the peak in the range (1200 – 1500) cm⁻¹ is assigned to the asymmetric stretching of B–O–B bond in trigonal BO₃ units. The B–O stretching frequency in tetrahedral BO₄ units gives peaks in the range (800 – 1200) cm⁻¹. The bending vibration of bridging oxygen (B–O–B) between BO₃ and BO₄ units are active and observed in the range of (600 – 800) cm⁻¹ [59]. Accordingly, small peak near 1026 cm⁻¹ corresponds to interstitial boron and stretching vibration of B–O bonds [35]. Small peak at 1319 cm⁻¹ is observed in accordance with the presence of BO₃ units. Peak at 1103 cm⁻¹ is attributed for BO₄ unit for BOT2 and BOT3. The broad peak at 1080 cm⁻¹ is attributed as red shift of the peak for BO₄ unit present in BOT1 [59].

The FTIR spectra suggests that (i) the vibrational and bending frequencies for B–O bonds are overlapped with the transmission of tin oxide and (ii) boron ions are supposed to occupy in the interstitial sites of SnO₂ crystal lattice as borate structures (BO₃ and BO₄) rather than in boroxol rings (B₂O₃). The higher oxygen deficiency caused by interstitial boron in BTO1, finds correlation with the decrease in vibra-

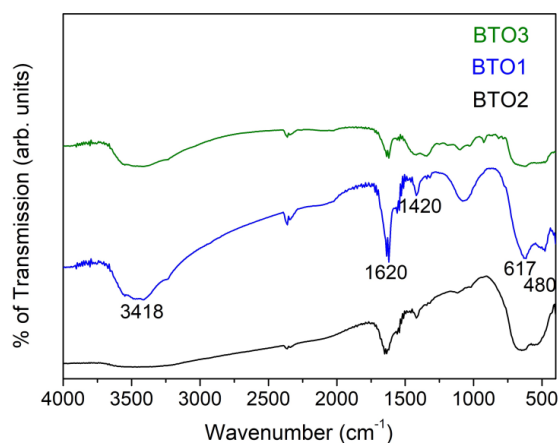


Figure 7. FTIR spectra of the synthesized three boron doped tin oxide samples.

tional frequency in accordance with the harmonic oscillator model [60]. This is also consistent with the XRPD studies (as in Table 1). Finally, the relative intensity of peaks at 1080 cm⁻¹, 1103 cm⁻¹ and 1319 cm⁻¹ in the three FTIR spectra supports that BOT1 possesses highest proportion of BO₄ unit than BO₃ units as compared to BOT2 and BOT3.

3.4 Antibacterial performance

The antibacterial activity of the boron doped tin oxide nanoparticles were investigated by Agar disc diffusion method against the Gram negative bacteria *E. Coli* (MCC2413), *E. Aerogenes* (MCC3092) and one Gram positive bacteria *S. Aureus*. The antimicrobial performances of the doped SnO₂ nanocrystals are shown in Fig. 8. It is, in general difficult to isolate the exact mechanism for differences in antibacterial effects for nanoparticles. Several authors [60–63] have identified reactive oxygen species generated oxidative stress and/or metal ion toxicity from the dissolved nanoparticles as the primary cause for antibacterial dissimilar activities. From the measured diameter of inhibition zones (in mm) as shown in Fig. 8, it is apparent that the samples BTO1 and BTO3 show enhanced antibacterial effects in both water and DMSO media. The B doped SnO₂ nanoparticles, BTO3, has a significant activity against both the Gram negative bacteria *E. Coli* and *E. Aerogenes*, whereas for BTO1, prepared in starch, has more influence on *E. Coli* and *S. Aureus*. In the earlier section, it has been shown from X-ray powder diffraction analysis that BTO1 has the smallest average crystallite size of ~ 12 nm and for BTO3, though having larger particle size, has anisotropic morphology. For the sample BTO2, the particle size is ~ 24 nm and have enhanced strain compared to BTO1 and BTO3. Earlier it has been shown that smaller particles, surface texture and morphology have stronger effects on the antibacterial activity for various nanoparticles [64–68]. Moreover, as the oxygen vacancy in the boron doped SnO₂ synthesized in glycerol medium BTO2 being smallest, more borate ions should be available in presence of water for BTO1 and BTO3, which goes in harmony with the observations from room temperature FTIR spectra as discussed in the earlier section. This in turn might further enhance their antimicrobial activity. Thus the observed differences in antibacterial response for these prepared boron doped tin oxide nanoparticles in different solvent may be due to smaller crystallite size, anisotropic microstructure and for

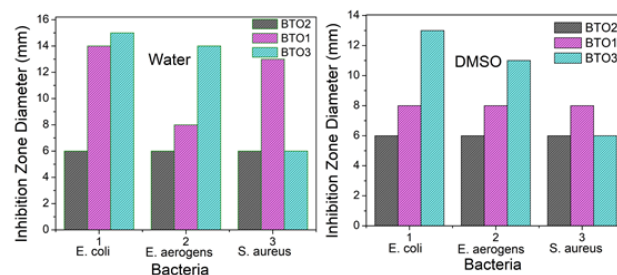


Figure 8. Histogram for the measured inhibition zone of BTO1, BTO2 and BTO3 samples in both water and DMSO media in presence of various pathogenic bacteria.

the presence of different oxygen vacancies in the material. Lattice disorder (first/second kind) does not have significant effect on the antibacterial activity.

4. Conclusion

Boron doped tin oxide nanocrystalline particles were synthesized by chemical route using sol-gel method. Three such doped samples were prepared using three different polyhydroxy alcohols starch, glycerol and PVA. Purity of the samples was confirmed by elemental analysis from EDX. Both scanning electron microscopy and X-ray powder diffraction profile revealed dissimilar microstructure in the as-prepared samples especially in the sample BTO3 prepared in PVA. The classical WH plot obtained from individual line profile analysis showed that the sample BTO3 has anisotropic microstructure, whereas it is isotropic for BTO1 and BTO2. For an in depth structural and microstructural study, whole profile fitting Rietveld analysis was carried out. Rietveld analysis confirmed formation of rutile structure for all the as-prepared samples with average coherent domain sizes 12 nm and 24 nm for BTO1 and BTO2 respectively. For BTO3 having anisotropic morphology, particle sizes are different along different directions ranging from 25 nm to 35 nm. BTO2 has the largest microstrain amongst the three $\sim 17 \times 10^{-4}$. BTO2 samples are further characterized by lattice disorder of second kind (paracrystalline disorder). Moreover XRPD analysis explored that due to boron incorporation in the SnO₂ lattice and smaller dimensions all three doped samples have oxygen deficiencies as corroborate from Raman and FTIR study. The antibacterial efficacies against some Gram-Positive and Gram-Negative bacteria for all these B-doped SnO₂ samples were different. This efficacy showed dependency on lower dimensions and anisotropic morphology of the nano-structured boron doped SnO₂ samples. This prepared boron ion doped tin dioxide nanoparticles may find applications in the field of photocatalytic activity.

Authors Contributions

Apurba Kanti Deb; Methodology: Apurba Kanti Deb, Achyutmohan Roy Chaudhury, Partha Chatterjee; Formal analysis and investigation: Sujay Munshi, Solanki Das, Debtanu Ghosh, Aritra Banerjee; Writing - original draft preparation: Apurba Kanti Deb; Writing - review and editing: Apurba Kanti Deb, Achyutmohan Roy Chaudhury, Partha Chatterjee; Supervision: Apurba Kanti Deb.

Availability of data and materials

The datasets generated and analyzed during the current study are available from the corresponding author upon reasonable request.

Conflict of Interests

The author declare that they have no known competing financial interests or personal relationships

that could have appeared to influence the work reported in this paper.

Open Access

This article is licensed under a Creative Commons Attribution 4.0 International License, which permits use, sharing, adaptation, distribution and reproduction in any medium or format, as long as you give appropriate credit to the original author(s) and the source, provide a link to the Creative Commons license, and indicate if changes were made. The images or other third party material in this article are included in the article's Creative Commons license, unless indicated otherwise in a credit line to the material. If material is not included in the article's Creative Commons license and your intended use is not permitted by statutory regulation or exceeds the permitted use, you will need to obtain permission directly from the OICC Press publisher. To view a copy of this license, visit <https://creativecommons.org/licenses/by/4.0>.

References

- [1] X. F. Wu, Y. J. Wang, L. J. Song, J. Z. Su, J. R. Zhang, Y. N. Jia, J. L. Shang, X. W. Nian, C. Y. Zhang, and X. G. Sun. "A yolk-shell Bi@ void@ SnO₂ photocatalyst with enhanced tetracycline degradation." *Journal of Materials Science: Materials in Electronics*, **30**:14987–14994, 2019. DOI: <https://doi.org/10.1007/s10854-019-01871-3>.
- [2] A. B. Ali Baig, V. Rathinam, and J. Palaninathan. "Photodegradation activity of yttrium-doped SnO₂ nanoparticles against methylene blue dye and antibacterial effects." *Applied Water Science*, **10**:76, 2020. DOI: <https://doi.org/10.1007/s13201-020-1143-1>.
- [3] S. Vallimeena and B. Helina. "2D hexagonal yttrium doped SnO₂ nanoplatelets for photocatalytic degradation." *Chemical Papers*, **77**:1683–1693, 2023. DOI: <https://doi.org/10.1007/s11696-022-02574-6>.
- [4] S. Das and V. Jayaraman. "SnO₂: A comprehensive review on structures and gas sensors." *Progress in Materials Science*, **66**:112–255, 2014. DOI: <https://doi.org/10.1016/j.pmatsci.2014.06.003>.
- [5] L. Yang, Z. Wang, X. Zhou, X. Wu, N. Han, and Y. Chen. "Synthesis of Pd-loaded mesoporous SnO₂ hollow spheres for highly sensitive and stable methane gas sensors." *RSC advances*, **8**:24268–24275, 2018. DOI: <https://doi.org/10.1039/c8ra03242d>.
- [6] P. S. Kolhe, P. M. Koinkar, N. Maiti, and K. M. Sonawane. "Synthesis of Ag doped SnO₂ thin films for the evaluation of H₂S gas sensing properties." *Physica B: Condensed Matter*, **524**:90–96, 2017. DOI: <https://doi.org/10.1016/j.physb.2017.07.056>.

- [7] Z. Zhang, C. Yin, L. Yang, J. Jiang, and Y. Guo. "Optimizing the gas sensing characteristics of Co-doped SnO₂ thin film based hydrogen sensor." *Journal of Alloys and Compounds*, **785**:819–825, 2019. DOI: <https://doi.org/10.1016/j.jallcom.2019.01.244>.
- [8] P. V. Kamat. "Dominance of metal oxides in the era of nanotechnology." *Journal of Physical Chemistry Letters*, **2**:839–840, 2011. DOI: <https://doi.org/10.1021/jz2002953>.
- [9] V. Zhelev, P. Petkov, P. Shindov, I. Bineva, S. Vasilev, V. Ilcheva, and T. Petkova. "As-doped SnO₂ thin films for use as large area position sensitive photodetector." *Thin Solid Films*, **653**:19–23, 2018. DOI: <https://doi.org/10.1016/j.tsf.2018.03.009>.
- [10] S. N. Sarangi, G. K. Pradhan, and D. Samal. "Band gap engineering in SnO₂ by Pb doping." *Journal of Alloys and Compounds*, **762**:16–20, 2018. DOI: <https://doi.org/10.1016/j.jallcom.2018.05.143>.
- [11] V. Vasu and A. Subrahmanyam. "Photovoltaic properties of indium tin oxide (ITO)/silicon junctions prepared by spray pyrolysis-dependence on oxidation time." *Semiconductor Science and Technology*, **7**:320, 1992. DOI: <https://doi.org/10.1088/0268-1242/7/3/006>.
- [12] Q. Tian, Y. Tian, Z. Zhang, L. Yang, and S. I. Hirano. "Facile synthesis of ultrasmall tin oxide nanoparticles embedded in carbon as high-performance anode for lithium-ion batteries." *Journal of Power Sources*, **269**:479–485, 2014. DOI: <https://doi.org/10.1016/j.jpowsour.2014.07.019>.
- [13] M. H. Chen, Z. C. Huang, G. T. Wu, G. M. Zhu, J. K. You, and Z. G. Lin. "Synthesis and characterization of SnO–carbon nanotube composite as anode material for lithium-ion batteries." *Materials Research Bulletin*, **38**:831–836, 2003. DOI: [https://doi.org/10.1016/S0025-5408\(03\)00063-1](https://doi.org/10.1016/S0025-5408(03)00063-1).
- [14] Y. Li, S. Zhu, Q. Liu, J. Gu, Z. Guo, Z. Chen, C. Feng, D. Zhang, and W. J. Moon. "Carbon-coated SnO₂@C with hierarchically porous structures and graphite layers inside for a high-performance lithium-ion battery." *Journal of Materials Chemistry*, **22**:2766–2773, 2012. DOI: <https://doi.org/10.1039/C1JM14290A>.
- [15] F. M. Courtel, E. A. Baranova, Y. Abu-Lebdeh, and I. J. Davidson. "In situ polyol-assisted synthesis of nano-SnO₂/carbon composite materials as anodes for lithium-ion batteries." *Journal of Power Sources*, **195**:2355–2361, 2010. DOI: <https://doi.org/10.1016/j.jpowsour.2009.10.086>.
- [16] S. Ito, Y. Makari, T. Kitamura, Y. Wada, and S. Yanagida. "Fabrication and characterization of mesoporous SnO₂/ZnO-composite electrodes for efficient dye solar cells." *Journal of Materials Chemistry*, **14**:385–390, 2004. DOI: <https://doi.org/10.1039/B311090G>.
- [17] K. Rubenis, S. Populoh, P. Thiel, S. Yoon, U. Müller, and J. Locs. "Thermoelectric properties of dense Sb-doped SnO₂ ceramics." *Journal of Alloys and Compounds*, **692**:515–521, 2017. DOI: <https://doi.org/10.1016/j.jallcom.2016.09.062>.
- [18] N. Ahmad, S. Khan, and M. M. Ansari. "Exploration of Raman spectroscopy, dielectric and magnetic properties of (Mn, Co) co-doped SnO₂ nanoparticles." *Physica B: Condensed Matter*, **558**:131–141, 2019. DOI: <https://doi.org/10.1016/j.physb.2019.01.044>.
- [19] A. Ahmed, M. N. Siddique, T. Ali, and P. Tripathi. "Defect assisted improved room temperature ferromagnetism in Ce doped SnO₂ nanoparticles." *Applied Surface Science*, **483**:463–471, 2019. DOI: <https://doi.org/10.1016/j.apsusc.2019.03.209>.
- [20] A. M. Roychaudhury, U. Debnath, S. Munshi, G. K. Basak, A. Dutta, S. Masanta, A. Singha, A. Banerjee, D. Ghosh, P. Chatterjee, and A. K. Deb. "Synthesis structural and anti-microbial characterization of nanostructured doped tin oxide." *Journal of Theoretical and Applied Physics*, **16**:162202, 2022. DOI: <https://doi.org/10.30495/jtap.162202>.
- [21] T. Minami. "Transparent conducting oxide semiconductors for transparent electrodes." *Semiconductor Science and Technology*, **20**:S35, 2005. DOI: <https://doi.org/10.1088/0268-1242/20/4/004>.
- [22] Z. Galazka, R. Uecker, D. Klimm, K. Irmscher, M. Pietsch, R. Schewski, M. Albrecht, A. Kwasniewski, S. Ganschow, D. Schulz, and C. Gugushev. "Growth, characterization, and properties of bulk SnO₂ single crystals." *Physica Status Solidi (a)*, **211**:66–73, 2014. DOI: <https://doi.org/10.1002/pssa.201330020>.
- [23] A. Schleife, J. B. Varley, F. Fuchs, C. Rödl, F. Bechstedt, P. Rinke, A. Janotti, and C. G. Van de Walle. "Tin dioxide from first principles: Quasiparticle electronic states and optical properties." *Physical Review B*, **83**:035116, 2011. DOI: <https://doi.org/10.1103/PhysRevB.83.035116>.
- [24] A. A. Firooz, A. R. Mahjoub, and A. A. Khodadadi. "Preparation of SnO₂ nanoparticles and nanorods by using a hydrothermal method at low temperature." *Materials Letters*, **62**:1789–1792, 2008. DOI: <https://doi.org/10.1016/j.matlet.2007.10.004>.
- [25] E. R. Leite, I. T. Weber, E. Longo, and J. A. Varela. "A new method to control particle size and particle size distribution of SnO₂ nanoparticles for gas sensor applications." *Advanced Materials*, **12**:965–968, 2000. DOI: [https://doi.org/10.1002/1521-4095\(200006\)12:13<965::AID-ADMA965>3.0.CO;2-7](https://doi.org/10.1002/1521-4095(200006)12:13<965::AID-ADMA965>3.0.CO;2-7).
- [26] C. Nayral, E. Viala, P. Fau, F. Senocq, J. C. Jumas, A. Maisonnat, and B. Chaudret. "Synthesis of tin and tin oxide nanoparticles of

- low size dispersity for application in gas sensing.”. *Chemistry–A European Journal*, **6**:4082–4090, 2000. DOI: [https://doi.org/10.1002/1521-3765\(20001117\)6:22;4082::aid-chem4082;3.0.co;2-s](https://doi.org/10.1002/1521-3765(20001117)6:22;4082::aid-chem4082;3.0.co;2-s).
- [27] G. Pang, S. Chen, Y. Koltypin, A. Zaban, S. Feng, and A. Gedanken. “Controlling the particle size of calcined SnO₂ nanocrystals.”. *Nano Letters*, **1**:723–726, 2001. DOI: <https://doi.org/10.1021/nl0156181>.
- [28] V. Subramanian, W. W. Burke, H. Zhu, and B. Wei. “Novel microwave synthesis of nanocrystalline SnO₂ and its electrochemical properties.”. *The Journal of Physical Chemistry C*, **112**:4550–4556, 2008. DOI: <https://doi.org/10.1021/jp711551p>.
- [29] T. Krishnakumar, R. Jayaprakash, M. Parthibavaran, A. R. Phani, V. N. Singh, and B. R. Mehta. “Microwave-assisted synthesis and investigation of SnO₂ nanoparticles.”. *Materials Letters*, **63**:896–898, 2009. DOI: <https://doi.org/10.1016/j.matlet.2009.01.032>.
- [30] Y. Ren, G. Zhao, and Y. Chen. “Fabrication of textured SnO₂: F thin films by spray pyrolysis.”. *Applied Surface Science*, **258**:914–918, 2011. DOI: <https://doi.org/10.1016/j.apsusc.2011.09.026>.
- [31] F. Paraguay-Delgado, W. Antunez-Flores, M. Miki-Yoshida, A. Aguilar-Elguezabal, P. Santiago, R. Diaz, and J. A. Ascencio. “Microstructural characterization of SnO₂ nanorods obtained by spray pyrolysis.”. *Microscopy and Microanalysis*, **10**:340–341, 2004. DOI: <https://doi.org/10.1017/S1431927604883119>.
- [32] G. H. Patel, S. H. Chaki, R. M. Kannaujiya, Z. R. Parekh, A. B. Hirpara, A. J. Khimani, and M. P. Deshpande. “Sol-gel synthesis and thermal characterization of SnO₂ nanoparticles.”. *Physica B: Condensed Matter*, **631**:412987, 2021. DOI: <https://doi.org/10.1016/j.physb.2021.412987>.
- [33] M. Aziz, S. S. Abbas, and W. R. Baharom. “Size-controlled synthesis of SnO₂ nanoparticles by sol-gel method.”. *Materials Letters*, **91**:31–34, 2013. DOI: <https://doi.org/10.1016/j.matlet.2012.09.079>.
- [34] B. Zhang, Y. Tian, J. X. Zhang, and W. Cai. “The structural and electrical studies on the Boron-doped SnO₂ films deposited by spray pyrolysis.”. *Vacuum*, **85**:986–989, 2011. DOI: <https://doi.org/10.1016/j.vacuum.2011.02.005>.
- [35] S. Kumar, Bhawna, S. K. Yadav, A. Gupta, R. Kumar, J. Ahmed, M. Chaudhary, Suhas, and V. Kumar. “B-doped SnO₂ nanoparticles: a new insight into the photocatalytic hydrogen generation by water splitting and degradation of dyes.”. *Environmental Science and Pollution Research*, **29**:47448–47461, 2022. DOI: <https://doi.org/10.1007/s11356-022-18946-0>.
- [36] Q. P. Tran, J. S. Fang, and T. S. Chin. “Optical properties and boron doping-induced conduction-type change in SnO₂ thin films.”. *Journal of Electronic Materials*, **45**:349–356, 2016. DOI: <https://doi.org/10.1007/s11664-015-4081-1>.
- [37] J. Zhi, M. Zhou, Z. Zhang, O. Reiser, and F. Huang. “Interstitial boron-doped mesoporous semiconductor oxides for ultratransparent energy storage.”. *Nature Communications*, **12**:445, 2021. DOI: <https://doi.org/10.1038/s41467-020-20352-4>.
- [38] X. B. Kong, F. Li, Z. N. Qi, L. Qi, and M. M. Yao. “Boron-doped tin dioxide films for environmental applications.”. *Surface Review and Letters*, **24**:1750059, 2017. DOI: <https://doi.org/10.1142/S0218625X17500597>.
- [39] J. Yu, Y. Wang, Y. Huang, X. Wang, J. Guo, J. Yang, and H. Zhao. “Structural and electronic properties of SnO₂ doped with non-metal elements.”. *Beilstein Journal of Nanotechnology*, **11**:1321–1328, 2020. DOI: <https://doi.org/10.3762/bjnano.11.116>.
- [40] P. P. Filippatos, N. Kelaidis, M. Vasilopoulou, D. Davazoglou, and A. Chroneos. “Impact of boron and indium doping on the structural, electronic and optical properties of SnO₂.”. *Scientific Reports*, **11**:13031, 2021. DOI: <https://doi.org/10.1038/s41598-021-92450-2>.
- [41] J. G. Van Berkum, G. J. Sprong, T. H. De Keijser, R. Delhez, and E. J. Sonneveld. “The optimum standard specimen for X-ray diffraction line-profile analysis.”. *Powder Diffraction*, **10**:129–139, 1995. DOI: <https://doi.org/10.1017/S0885715600014512>.
- [42] L. Lutterotti, S. Matthies, and H. Wenk. “MAUD: a friendly Java program for material analysis using diffraction.”. *CPD Newsletter*, **21**:14–15, 1999.
- [43] A. K. Deb, P. Chatterjee, and S. P. Sen Gupta. “An X-ray diffraction study on dislocation microstructure of as-prepared Al–Al₂O₃ composites.”. *Actamaterialia*, **52**:2755–2764, 2004. DOI: <https://doi.org/10.1016/j.actamat.2004.02.023>.
- [44] P. Thompson, D. E. Cox, and J. B. Hastings. “Rietveld refinement of Debye–Scherrer synchrotron X-ray data from Al₂O₃.”. *Journal of Applied Crystallography*, **20**:79–83, 1987. DOI: <https://doi.org/10.1107/S0021889887087090>.
- [45] N. C. Popa. “The (hkl) dependence of diffraction-line broadening caused by strain and size for all Laue groups in Rietveld refinement.”. *Journal of Applied Crystallography*, **31**:176–180, 1998. DOI: <https://doi.org/10.1107/S0021889897009795>.
- [46] K. Jurkiewicz, M. Kamiński, W. Glajcar, N. Woźnica, F. Julienne, P. Bartczak, J. Polański, J. Lelatko, M. Zubko, and A. Burian. “Paracrystalline

- structure of gold, silver, palladium and platinum nanoparticles.”. *Journal of Applied Crystallography*, **51**:411–419, 2018. DOI: <https://doi.org/10.1107/S1600576718001723>.
- [47] R. Hosemann, W. Wilke, and F. B. Calleja. “Twist-Kornsgrenzen und andere parakristalline Gitterstörungen in Polyäthylen-Einkristallen.”. *Acta Crystallographica*, **21**:118–123, 1966. DOI: <https://doi.org/10.1107/S0365110X66002408>.
- [48] A. Dieguez, A. Romano-Rodríguez, A. Vila, and J. R. Morante. “The complete Raman spectrum of nanometric SnO₂ particles.”. *Journal of Applied Physics*, **90**:1550–1557, 2001. DOI: <https://doi.org/10.1063/1.1385573>.
- [49] A. Ahmed, M. N. Siddique, T. Ali, and P. Tripathi. “Defect assisted improved room temperature ferromagnetism in Ce doped SnO₂ nanoparticles.”. *Applied Surface Science*, **483**:463–471, 2019. DOI: <https://doi.org/10.1016/j.apsusc.2019.03.209>.
- [50] S. G. Ansari, M. A. Dar, M. S. Dhage, Y. S. Kim, Z. A. Ansari, A. Al-Hajry, and H. S. Shin. “A novel method for preparing stoichiometric SnO₂ thin films at low temperature.”. *Review of Scientific Instruments*, **80**:045112, 2009. DOI: <https://doi.org/10.1063/1.3115222>.
- [51] F. Paraguay-Delgado, F. C. Vasquez, J. T. Holguín-Momaca, C. R. Santillán-Rodríguez, J. A. Matutes-Aquino, and S. F. Olive-Méndez. “Room-temperature ferromagnetism and morphology evolution of SnO₂ flower-like microparticles by Zn-doping.”. *Journal of Magnetism and Magnetic Materials*, **476**:183–187, 2019. DOI: <https://doi.org/10.1016/j.jmmm.2018.12.102>.
- [52] L. Z. Liua nd J. Q. Xu, X. L. Wu, T. H. Li, J. C. Shen, and P. K. Chu. “Optical identification of oxygen vacancy types in SnO₂nanocrystals.”. *Applied Physics Letters*, **102**:031916, 2013. DOI: <https://doi.org/10.1063/1.4789538>.
- [53] M. Guan, X. Zhao, L. Duan, M. Cao, W. Guo, J. Liu, and W. Zhang. “Controlled synthesis of SnO₂ nanostructures with different morphologies and the influence on photocatalysis properties.”. *Journal of Applied Physics*, **114**:114302, 2013. DOI: <https://doi.org/10.1063/1.4821140>.
- [54] S. Das, S. Kar, and S. Chaudhuri. “Optical properties of SnO₂ nanoparticles and nanorods synthesized by solvothermal process.”. *Journal of Applied Physics*, **99**:114303, 2006. DOI: <https://doi.org/10.1063/1.2200449>.
- [55] P. Sangeetha, V. Sasirekha, and V. Ramakrishnan. “Micro-Raman investigation of tin dioxide nanostructured material based on annealing effect.”. *Journal of Raman Spectroscopy*, **42**:1634–1639, 2011. DOI: <https://doi.org/10.1002/jrs.2919>.
- [56] F. H. Aragon, J. A. Coaquira, P. Hidalgo, S. W. Da Silva, S. L. Brito, D. Gouvêa, and P. C. Morais. “Evidences of the evolution from solid solution to surface segregation in Ni-doped SnO₂ nanoparticles using Raman spectroscopy.”. *Journal of Raman Spectroscopy*, **42**:1081–1086, 2011. DOI: <https://doi.org/10.1002/jrs.2802>.
- [57] A. Ahmed, M. N. Siddique, T. Ali, and P. Tripathi. “Defect assisted improved room temperature ferromagnetism in Ce doped SnO₂ nanoparticles.”. *Applied Surface Science*, **483**:463–471, 2019. DOI: <https://doi.org/10.1016/j.apsusc.2019.03.209>.
- [58] S. Uma, J. Singh, and V. Thakral. “Facile room temperature ion-exchange synthesis of Sn²⁺ incorporated pyrochlore-type oxides and their photocatalytic activities.”. *Inorganic Chemistry*, **48**:11624–11630, 2009. DOI: <https://doi.org/10.1021/ic901658w>.
- [59] C. C. Zhang, X. Gao, and B. Yilmaz. “Development of FTIR spectroscopy methodology for characterization of boron species in FCC catalysts.”. *Catalysts*, **10**:1327, 2020. DOI: <https://doi.org/10.3390/catal10111327>.
- [60] A. Besinis, T. De Peralta, and R. D. Handy. “The antibacterial effects of silver, titanium dioxide and silica dioxide nanoparticles compared to the dental disinfectant chlorhexidine on Streptococcus mutans using a suite of bioassays.”. *Nanotoxicology*, **8**:1–6, 2014. DOI: <https://doi.org/10.3109/17435390.2012.742935>.
- [61] S. Sarwar, S. Chakraborti, S. Bera, I. A. Sheikh, K. M. Hoque, and P. Chakrabarti. “The antimicrobial activity of ZnO nanoparticles against Vibrio cholerae: Variation in response depends on biotype.”. *Nanomedicine: Nanotechnology, Biology and Medicine*, **12**:1499–1509, 2016. DOI: <https://doi.org/10.1016/j.nano.2016.02.006>.
- [62] D. Touati. “Iron and oxidative stress in bacteria.”. *Archives of Biochemistry and Biophysics*, **373**:1–6, 2000. DOI: <https://doi.org/10.1006/abbi.1999.1518>.
- [63] S. J. Stohs and D. Bagchi. “Oxidative mechanisms in the toxicity of metal ions.”. *Free Radical Biology and Medicine*, **18**:321–336, 1995. DOI: [https://doi.org/10.1016/0891-5849\(94\)00159-H](https://doi.org/10.1016/0891-5849(94)00159-H).
- [64] T. K. Jana, S. K. Jana, A. Kumar, K. De, R. Maiti, A. K. Mandal, T. Chatterjee, B. K. Chatterjee, P. Chakrabarti, and K. Chatterjee. “The antibacterial and anticancer properties of zinc oxide coated iron oxide nanotextured composites.”. *Colloids and Surfaces B: Biointerfaces*, **177**:512–519, 2019. DOI: <https://doi.org/10.1016/j.colsurfb.2019.02.041>.
- [65] T. Chatterjee, B. K. Chatterjee, and P. Chakrabarti. “Modelling of growth kinetics of Vibrio cholerae in presence of gold nanoparticles: Effect of size and morphology.”. *Scientific Reports*, **7**:9671, 2017. DOI: <https://doi.org/10.1038/s41598-017-09357-0>.

- [66] T. K. Jana, S. K. Maji, A. Pal, R. P. Maiti, T. K. Dolai, and K. Chatterjee. “Photocatalytic and antibacterial activity of cadmium sulphide/zinc oxide nanocomposite with varied morphology.”. *Journal of Colloid and Interface Science*, **480**:9–16, 2016. DOI: <https://doi.org/10.1016/j.jcis.2016.06.073>.
- [67] G. Mohammadi, H. Valizadeh, M. Barzegar-Jalali, F. Lotfipour, K. Adibkia, M. Milani, M. Azhdarzadeh, F. Kiafar, and A. Nokhodchi. “Development of azithromycin–PLGA nanoparticles: Physicochemical characterization and antibacterial effect against *Salmonella typhi*.”. *Colloids and Surfaces B: Biointerfaces*, **80**:34–39, 2010. DOI: <https://doi.org/10.1016/j.colsurfb.2010.05.027>.
- [68] S. Pal, Y. K. Tak, and J. M. Song. “Does the antibacterial activity of silver nanoparticles depend on the shape of the nanoparticle? A study of the gram-negative bacterium *Escherichia coli*.”. *Applied and Environmental Microbiology*, **73**:1712–1720, 2007. DOI: <https://doi.org/10.1128/AEM.02218-06>.